Extraction of interaction parameters for α-RuCl$_3$ from neutron data using machine learning

Anjana M. Samarakoon [1,2,3,*] Pontus Laurell [4,5,6] Christian Balz,[2,7] Arnab Banerjee,[2,8] Paula Lampen-Kelley,[9,10]
David Mandrus,[9,10] Stephen E. Nagler [2,11] Satoshi Okamoto,[10,11] and D. Alan Tennant[1,6,10,11]

[1]*Shull-Wollan Center, Oak Ridge National Laboratory, Oak Ridge, Tennessee 37831, USA*
[2]*Neutron Scattering Division, Oak Ridge National Laboratory, Oak Ridge, Tennessee 37831, USA*
[3]*Materials Science Division, Argonne National Laboratory, Lemont, Illinois 60439, USA*
[4]*Center for Nanophase Materials Sciences, Oak Ridge National Laboratory, Oak Ridge, Tennessee 37831, USA*
[5]*Computational Sciences and Engineering Division, Oak Ridge National Laboratory, Oak Ridge, Tennessee 37831, USA*
[6]*Department of Physics and Astronomy, University of Tennessee, Knoxville, Tennessee 37996, USA*
[7]*ISIS Neutron and Muon Source, Rutherford Appleton Laboratory, Didcot, OX11 0QX, United Kingdom*
[8]*Department of Physics and Astronomy, Purdue University, West Lafayette, Indiana 47906, USA*
[9]*Department of Materials Science and Engineering, University of Tennessee, Knoxville, Tennessee 37996, USA*
[10]*Materials Science and Technology Division, Oak Ridge National Laboratory, Oak Ridge, Tennessee 37831, USA*
[11]*Quantum Science Center, Oak Ridge National Laboratory, Oak Ridge, Tennessee 37831, USA*

Single-crystal inelastic neutron-scattering (INS) data contain rich information about the structure and dynamics of a material. Yet the challenge of matching sophisticated theoretical models with large data volumes is compounded by computational complexity and the ill-posed nature of the inverse scattering problem. Here we utilize a novel machine-learning (ML)-assisted framework featuring multiple neural network architectures to address this via high-dimensional modeling and numerical methods. A comprehensive data set of diffraction and INS measured on the Kitaev material $\alpha - RuCl_3$ is processed to extract its Hamiltonian. Semiclassical Landau-Lifshitz dynamics and Monte-Carlo simulations were employed to explore the parameter space of an extended Kitaev-Heisenberg Hamiltonian. A ML-assisted iterative algorithm was developed to map the uncertainty manifold to match experimental data, a nonlinear autoencoder was used to undertake information compression, and radial basis networks were utilized as fast surrogates for diffraction and dynamics simulations to predict potential spin Hamiltonians with uncertainty. Exact diagonalization calculations were employed to assess the impact of quantum fluctuations on the selected parameters around the best prediction.

Introduction. Highly frustrated quantum systems are important routes to realizing exotic ground states and excitations. They are proposed to host states ranging from long-range entangled quantum spin liquids (QSLs) with nonlocal excitations to quantum spin ices with emergent photons [1–3]. Recently, the two-dimensional (2D) honeycomb spin-1/2 material α-RuCl$_3$ [Fig. 1(a)] has garnered particular attention after being reported [4–11] as a leading candidate [12–14] for realization of the Kitaev model—an exactly solvable QSL Hamiltonian [15,16]. The Kitaev model is a spin network with competing bond-dependent interactions and hosts a topological QSL ground state that supports two types of fractionalized excitations: visons, which are excitations of the emergent flux, and deconfined Majorana fermions. These quasiparticles are predicted to show non-Abelian statistics, suggesting potential applications in, e.g., topological quantum computing [17]. Recently, theoretical propositions have been made for interferometers utilizing their braiding statistics as a precursor to undertaking quantum operations [18,19]. Meanwhile, however, the experimental situation regarding the quasiparticles in α-RuCl$_3$ remains inconclusive primarily due to difficulties in determining the precise nature of the spin couplings in the material and to what extent these destabilize the QSL state in zero and applied magnetic fields.

Experiments have revealed evidence that α-RuCl$_3$ is close to the Kitaev QSL[12,13,23,24]. At low temperatures and magnetic fields it orders magnetically in a zigzag (Z.Z.) structure [6,25–27], implying the presence of symmetry-allowed interactions additional to the Kitaev Hamiltonian, as is generically predicted by theory [20,28–30]. Inelastic neutron scattering (INS) shows scattering dominated by continua at the zone center [7–11], interpreted as originating from underlying fractional Majorana excitations or from incoherent excitations due to magnon decay [31–33]; both related to strongly fluctuating quantum states. Similarly, Raman scattering shows a broad scattering continuum at the zone center [5,34–37] and a fermionic temperature dependence interpreted as indicating fractional excitations. The
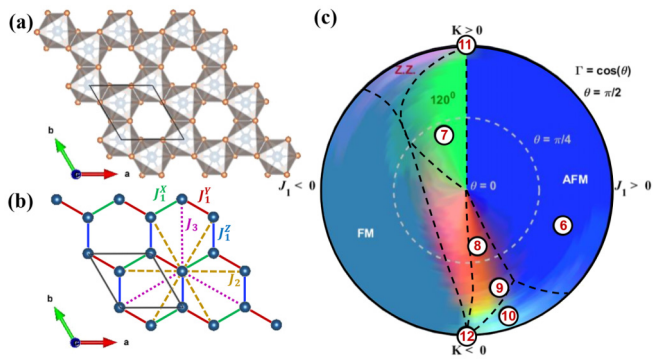
FIG. 1. (a) The α-RuCl$_3$ crystal structure, consisting of Ru sites at centers of edge-sharing Cl octahedra. (b) The magnetism is due to Ru^{3+} ions, which form a honeycomb lattice. Nearest-, second-nearest-, and third-nearest-neighbor bonds are indicated by solid, dashed, and dotted lines, respectively. Anisotropic nearest-neighbor interactions are considered as given in Eq. (1). (c) Machine-learned phase diagram for the $J_1 - K - \Gamma$ model at $T = 1$ K with theoretical phase boundaries from Ref. [20] overlaid in black dashed lines. The different colors, which represent different structure factors $S(\mathbf{Q})$, are predicted by a trained neural network as explained in the main text. Numbered points correspond to $S(\mathbf{Q})$ shown in Fig. 2(b). The identified phases include ferromagnetic [FM], Néel [AFM], 120°, and zigzag [Z.Z.] orders.

Z.Z. order melts in a narrow range of applied in-plane magnetic fields, possibly inducing a QSL state [10,11,38–40]. Oscillations of the thermal conductivity were also observed in this field range, suggesting the presence of a Fermi surface [41–43]. Perhaps the most striking reports are those of a half-integer-quantized thermal Hall effect in the same field range [44–46]. Additional experimental evidence for Kitaev interactions in α-RuCl$_3$ has been reported using, e.g., inelastic x-ray scattering [47], thermodynamical [8,48–51], NMR [39,52], electron-spin resonance [53], microwave absorption [54], thermal transport [55,56], and THz spectroscopy [57–61] techniques.

The complexity of magnetic interactions in RuCl$_3$ has hindered determination of an underlying model. Various groups have fit or derived proposed Hamiltonian parameters for the material [6,9,23,24,29–31,59,60,62–71], but these studies disagree significantly regarding which interactions are present and on values of specific interaction parameters [33,72,73]. Part of the reason for this lack of agreement is that many experimental fits have relied on linear spin-wave theory (LSWT), which cannot account for the quantum fluctuations inherent to α-RuCl$_3$. However, the more central issue is that a comparatively large set of weak perturbations is possible, which can significantly modify the magnetic ordering, dynamics, and thermal properties of Kitaev materials. With such a high-dimensional parameter space, comparing modeling with experimental data leaves a great deal of uncertainty unless comprehensive enough to explore the range of possible interactions, an approach which is absent to date.

Scattering data contain considerable information on the magnetic states and interactions in materials. A difficult step in the quantification of models has been inversion from measured data to a model—the so-called inverse scattering problem—which is usually ill posed due to loss of phase

information. In this regard, machine learning (ML) [74,75] has shown promising results [76–80]. Here we combine ML approaches with large-scale semiclassical simulations (SCSs) [80]. ML-SCS techniques have been used to successfully extract couplings from diffuse neutron-scattering data and yielded significant insight by mapping the physical behavior in high-dimensional interaction spaces of materials [80,81]. We extend these methods to include dynamics data for α-RuCl$_3$, allowing a comprehensive fit.

Experiments. Neutron diffraction studies were performed at the Spallation Neutron Source (SNS) [82] using the CORELLI beamline [83]. A 125-mg α-RuCl$_3$ crystal was mounted on an aluminium plate and aligned with the $[h, 0, l]$ plane horizontal. The crystal was rotated through 170° in 2° steps about the vertical axis. The temperature of the measurement was 2 K and the perpendicular wave vector transfer was integrated in the range $l = [0.92, 1.08]$ r.l.u.. The diffraction data was previously published as Supplemental Fig. S2(a) in Ref. [10]. It was reduced as total scattering $S(\mathbf{Q})$, i.e., not using the cross-correlation algorithm that may be used for estimating purely elastic scattering $S(\mathbf{Q}, \omega = 0)$.

INS was performed on a 0.7 g single crystal, which was sealed in a thin-walled aluminium can with 1 atmosphere of helium gas for thermal contact. Measurements at 4 K were carried out using the SEQUOIA spectrometer [84,85] at the SNS. The incident energy was set to $E_i = 22.5$ meV. The crystal was mounted with $[h, 0, 0]$ and $[0, 0, l]$ axes in the horizontal plane, and the orthogonal $[0.5k, -k, 0]$ axis pointing vertically upward. Data were collected by rotating the crystal about the vertical axis over 290° in 1° steps. The data are integrated over the range $[0, 0, l] = [-3.5, 3.5]$.

Modeling. We consider a generalized spin-1/2 Kitaev-Heisenberg spin (local moment) Hamiltonian,

$$H = \sum_{\gamma=X,Y,Z} \sum_{\langle i,j \rangle^\gamma} \mathbf{S}_i \cdot J_1^\gamma \cdot \mathbf{S}_j$$
$$+ J_2 \sum_{\langle\langle i,j \rangle\rangle} \mathbf{S}_i \cdot \mathbf{S}_j + J_3 \sum_{\langle\langle\langle i,j \rangle\rangle\rangle} \mathbf{S}_i \cdot \mathbf{S}_j, \quad (1)$$

on the honeycomb lattice [Fig. 1(b)], which is expected to capture relevant interactions in the 2D plane; $\langle \ldots \rangle$, $\langle\langle \ldots \rangle\rangle$, and $\langle\langle\langle \ldots \rangle\rangle\rangle$ represent nearest, next-nearest and third-nearest neighbors, respectively, and

$$J_1^X = \begin{bmatrix} J_1 + K & 0 & 0 \\ 0 & J_1 & \Gamma \\ 0 & \Gamma & J_1 \end{bmatrix}, \quad J_1^Y = \begin{bmatrix} J_1 & 0 & \Gamma \\ 0 & J_1 + K & 0 \\ \Gamma & 0 & J_1 \end{bmatrix},$$

$$J_1^Z = \begin{bmatrix} J_1 & \Gamma & 0 \\ \Gamma & J_1 & 0 \\ 0 & 0 & J_1 + K \end{bmatrix}.$$

Exchange matrices are defined in the $\{X, Y, Z\}$ coordinate system with principal axes along mutually orthogonal normal vectors of three nearest-neighbor Ru-Cl-Ru-Cl plaquettes. Our model includes nearest-neighbor Heisenberg (J_1), Kitaev (K), and symmetric off-diagonal Gamma (Γ) interactions, as well as second- (J_2) and third-nearest (J_3) Heisenberg exchanges. For $J_2 = 0$ it reduces to a proposed minimal model for α-RuCl$_3$ [29]. Equation (1) is, however, restricted compared with some proposed models, notably neglecting,
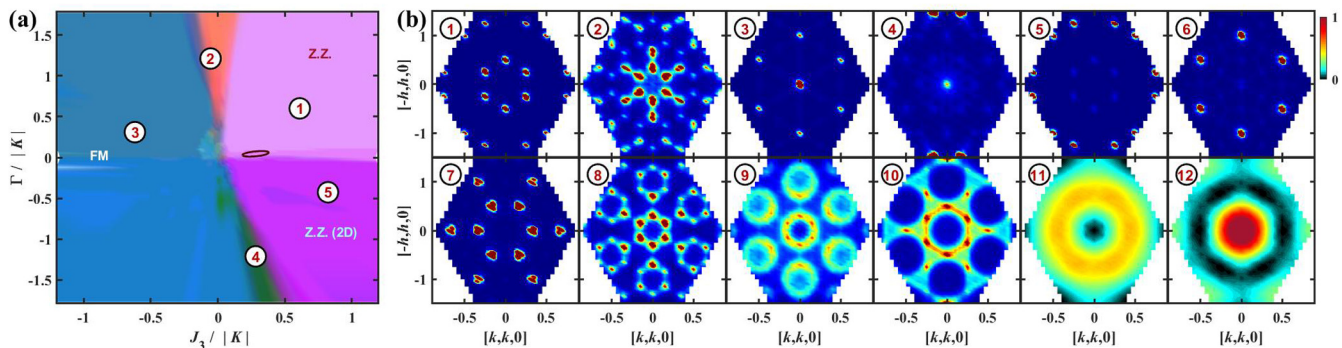
FIG. 2. (a) Machine-learned phase map varying $\Gamma/|K|$ and $J_3/|K|$ through the optimal solution for α-RuCl$_3$ at fixed $J_1/|K| = -0.1$ and $J_2/|K| = 0$, with $K < 0$. Labeled phases include FM, Z.Z., and planar zigzag [Z.Z. (2D)] orders. The ellipsoidal approximation to the optimal solution is marked in panel (a) in dark red. Due to uneven sampling of the IMA process from which the data were taken, the prediction accuracy varies in parameter space resulting in a blotchy appearance. The different colors, which represent different structure factors $S(\mathbf{Q})$, are predicted by a trained neural network as explained in the main text. Panel (b) shows the surrogate predicted neutron structure factor, $S^{\mathrm{Sur}}(\mathbf{Q})$, at numbered locations indicated in (a) and Fig. 1(c). Corresponding spin structures for the long-range-ordered phases labeled 1 and 3–7 are given in the SM [21]. Note that Z.Z. and Z.Z. (2D) have similar long-range order but along different spin-orientation directions. This occurs because, as discussed in Ref. [22], when $K < 0$ the spin orientation in Z.Z. ground states depends on the sign of Γ. Due to the neutron spin polarization factor, the two $S(\mathbf{Q})$ are different in the shown plane despite yielding the same trace over spin correlations, $\sum_\alpha S^{\alpha\alpha}(\mathbf{Q})$. Some of the diffuse $S(\mathbf{Q})$, taken at either phase boundaries or critical points, are also shown. The $S(\mathbf{Q})$ labeled 11 and 12 are for the pure AFM and FM Kitaev models.

e.g., interlayer exchange [11,23,86] and the Γ' term associated with trigonal distortion [20]. There are conflicting reports as to the magnitude of Γ' [33,70,73], such that neglecting it may not be fully justified. Nevertheless, this choice of Hamiltonian allows us to reduce the computational complexity and to clearly present our proposed method and its capabilities. We note that ML-SCS techniques have been used to theoretically explore phase diagrams of related Hamiltonians [87,88].

To simulate spin structure and dynamics, Metropolis (Monte Carlo) sampling [89] and Landau-Lifshitz (LL) dynamics are used [80]. This incorporates effects beyond LSWT while achieving sufficiently good performance to allow generating a sufficient amount of training data. Spin-1/2 operators in Eq. (1) are approximated by classical spin vectors subject to semiclassical normalization, $|\mathbf{S}_i| = \sqrt{S(S+1)}$. Metropolis sampling is carried out at a fixed temperature of 1 K, yielding well-thermalized spin configurations. Spin dynamics is governed by the usual LL equations of motion; see Supplemental Material (SM) [21]. The LL equation is solved numerically using a fourth-order Runge-Kutta algorithm with adaptive step size [90]. We use a cluster of 20×20 unit cells with periodic boundary conditions [21]. Neutron magnetic form factor for Ru^{3+}, polarization factors, and instrumental resolution are accounted for to match with experimental data. Figure 2(b) shows sampling of diffuse scattering at different locations in parameter space. The simulated scattering, $S^{\mathrm{sim}}(\mathbf{Q})$, shows complex behavior, reflecting the rich physics of Eq. (1).

ML method. Our method builds on Ref. [81], which recently demonstrated that an ML-integrated method can be used with the experimental static structure factor, $S^{\mathrm{exp}}(\mathbf{Q})$, to extract Hamiltonian parameters from diffuse scattering data on a spin ice. Unlike spin ice, α-RuCl3 shows a magnetic diffraction pattern with sharp Bragg peaks associated with long-range order, which does not sufficiently constrain the model parameters. Thus we extend the method to also account for the dynamical structure factor $S^{\mathrm{exp}}(\mathbf{Q}, \omega)$ from

spectroscopy. Although finding a single model to explain the entire 4D scattering is a formidable task; doing so should help avoid fits biased by incomplete information.

A ML-integrated workflow with autoencoder training and global optimization was used to simultaneously fit for both $S(\mathbf{Q})$ and $S(\mathbf{Q}, \omega)$. A 4D hyperparameter space, $\{p\}$, was explored to learn the uncertainty manifold in the 5D parameter space $\{J_1, K, \Gamma, J_2, J_3\}$ [21] using a variant of the efficient global optimization algorithm [81,91] which we call the iterative mapping algorithm (IMA). Autoencoders are unsupervised artificial neural networks with architecture as shown in Fig. 3(a). We train two autoencoders [21] with either $S(\mathbf{Q})$ or $S(\mathbf{Q}, \omega)$. The *Encoder* takes a linearized version of the structure factor $S(\nu)$ [$\nu = \mathbf{Q}$ or $\nu = \mathbf{Q}, \omega$] and outputs a compressed representation, $S(L)$, reducing the input dimensionality $N_\nu = 10^6 - 10^8$ pixels down to $N_L = 10^0 - 10^2$. The *Decoder* is a contrary network, which projects $S(L)$ back to the original dimensionality and predicts $S_{\mathrm{AE}}(\nu)$. Our *Encoders* and *Decoders* are designed to be symmetrical, and the numbers of layers are tuned as described in Ref. [21].

Two separate radial basis networks (RBNs) [92], shown in Fig. 3(b), provide *generator* networks (GN) to approximately map the Hamiltonian space $H(\{p\})$ directly to latent space, $\mathcal{L}_\nu$; see Ref. [21] for training details. The GN provides surrogate calculations to bypass the computationally expensive direct solver, allowing exhaustive searches for parameter space mapping as illustrated in Fig. 3(c). GN predictions depend on the degree of training of the network, the topography of the parameter space, and the sampling sparsity. They do not fully replace simulations and should not be used to draw conclusions when detailed information is needed. Complete surrogates predicting structure factors, $S^{\mathrm{sur}}(\nu)$, are constructed by linking the GN with the corresponding Decoder. These surrogates can also be used as low-cost estimators in the IMA as an alternative to the Gaussian process regression in Ref. [81].
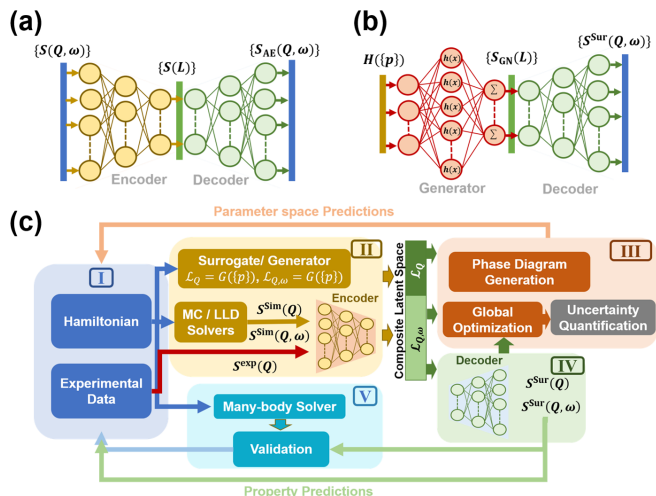
FIG. 3. Schematic illustrations of ML methods. (a) Autoencoder architecture used to compress 3D/4D $S(\mathbf{Q})/S(\mathbf{Q}, \omega)$ volumes into a much lower dimensionality. The autoencoder is trained with simulated data to reproduce the input. The architecture consists of two networks: *Encoder* and *Decoder*. The output of *Encoder* contains a compressed (latent space) representation, $S(L)$ of the input $S(\mathbf{Q}, \omega)$. *Decoder* decompresses $S(L)$ into a filtered structure factor, $S_{AE}(\mathbf{Q}, \omega)$, with the original dimensionality. (b) Schematic design of constructing the surrogate for predicting $S(\mathbf{Q})/S(\mathbf{Q}, \omega)$ given a set of model parameters. The surrogate comprises a RBN as the *Generator* mapping parameter space, $H(\{p\})$, to latent space $S_{GN}(L)$ and a *Decoder* to reconstruct $S(\mathbf{Q})/S(\mathbf{Q}, \omega)$ from latent space representations. The GN is trained with simulated data for evaluated parameter sets $\{p\}$ as input and corresponding $S(L)$ as target. (c) The ML workflow implemented here to integrate scattering experiments with theory, and extract model parameters and phase-diagram information.

FIG. 4. Optimal solution for α-RuCl$_3$. Panel (a) shows a slice of $\hat{\chi}^2_{S(\mathbf{Q})}$ as a function of $J_3/|K|$ and $\Gamma/|K|$. The problem is strongly underdetermined when only $S(\mathbf{Q})$ is taken into account, with a flat fitness landscape indicating many possible solutions. (b) Same slice for $\hat{\chi}^2_{S(\mathbf{Q},\omega)}$. The fitness landscape remains relatively flat when only $S(\mathbf{Q}, \omega)$ is accounted for. (c) Slice for the combined $\hat{\chi}^2_{Com}$ function, which accounts for both statics and dynamics. An ellipsoidal approximation to the optimal regions is shown in pink in panels (a), (b), and (c). Panel (d) shows line cuts of $\hat{\chi}^2_{Com}$ for individual parameters by fixing other parameters to their optimal values.

As Fig. 3(c) schematically shows, the workflow can be split into five sections: (I) Scattering experiment and hypothesis, (II) parameter space exploration and information compression, (III) structure or property predictions, (IV) parameter space predictions, and (V) validation of SCS results using a quantum many-body solver. The workflow is similar to that proposed in Ref. [93], but here we add step V and use a composite latent space $\mathcal{L}_{\mathbf{Q}} \cup \mathcal{L}_{\mathbf{Q},\omega}$. The latent space forms the backbone of the operation into which experimental data, simulations, and predictions from GN feed and from which structure, property, and model parameters are predicted.

ML predictions. The $S(\mathbf{Q})$ [and consequently $S(L)$] provides natural classification of phases, as the correlations of the system are encoded [93]. A high-dimensional graphical phase diagram can be constructed easily by projecting Q space into a latent space of $N_L = 3$ as suggested in Ref. [93]. An architecture of three intermediate layers with 300-3-300 logistic neurons [activation function as $f(x) = 1/(1 + e^{-x})$] was empirically found to have the highest performance for the $S^{sim}(\mathbf{Q})$.

Two phase diagrams are plotted in Figs. 1(c) and 2(a). Phases are indicated by color derived by treating latent vectors as RGB color components [80]. Figure 1(c) corresponds to the $J_2 = J_3 = 0$ hyperplane and uses the parametrization [20] $J_1 = \sin\theta\cos\phi$, $K = \sin\theta\sin\phi$, $\Gamma = \cos\theta$, where the energy scale is fixed according to $1 = \sqrt{J_1^2 + K^2 + \Gamma^2}$. Overlaid

dashed black lines indicate the theoretically predicted phase diagram. We note that typically our method does not find sharp transitions, so our results are not phase diagrams in a strict sense. Nevertheless, the excellent agreement between Fig. 1(c) and the phase diagram derived in Ref. [20] shows the merit of the approach. Figure 2(a) shows the phase diagram in a slice around the optimal solution we find for α-RuCl$_3$ (see Fig. 4 and later discussion). Figure 2(b) indicates the scattering at various points in the two phase diagrams.

To fit experimental scattering data and map uncertainty in the 5D parameter space, we employed IMA with cost function $\hat{\chi}^2_{Com} = \hat{\chi}^2_{S(\mathbf{Q})} \times \hat{\chi}^2_{S(\mathbf{Q},\omega)}$, where the $\hat{\chi}^2_{S(\nu)}$ are low-cost estimators defined in the SM [21]. IMA samples the parameter space iteratively subject to $\hat{\chi}^2_{Com} \leqslant C_{Com}$. The threshold value C_{Com} is iteratively reduced to a final value. The Autoencoders and GN are retrained at the end of each iteration. Thus the predictability of the networks becomes reliable toward the minimum of $\hat{\chi}^2_{Com}$.

Results and Discussion. Figure 4 shows slices and cuts of the final $\hat{\chi}^2_{Com}$ in parameter space. Due to uncertainties in the data, minimizing $\hat{\chi}^2_{Com}$ leads to a region of potential fits indicated by the ellipsoid in panels (a)–(c). Additional Hamiltonian terms may need to be included in the modeling to capture all relevant interactions and achieve higher fitting certainty. This restriction aside, we have identified several parameter sets with particularly low $\hat{\chi}^2_{Com}$, and these were investigated more closely. Figure 5 shows $S(\mathbf{Q})$ and $S(\mathbf{Q}, \omega)$
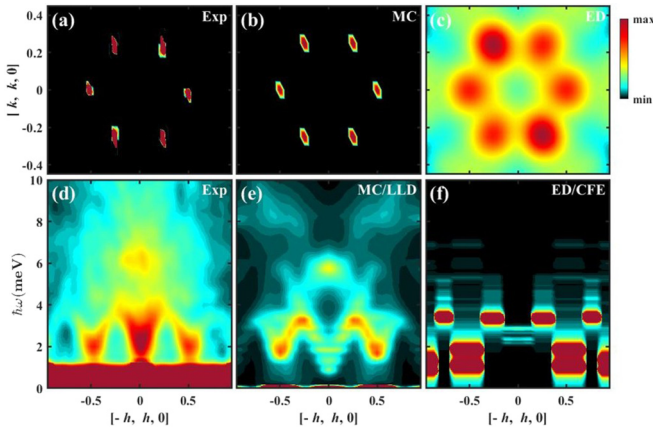
FIG. 5. Top row: (a) Experimental and (b, c) theoretical static spin structure factors calculated using (b) MC simulation and (c) Lanczos ED for the optimized Hamiltonian parameters. All methods find peaks at the M points, reflecting the Z.Z. ordering. Bottom row: Inelastic scattering from (d) experiment, (e) LLD, and (f) Lanczos ED for the same parameter set.

from experiment, LL simulation, and Lanczos exact diagonalization (ED) for the optimized parameter set: $J_1 = -0.4 \pm 0.4$ meV, $K = -5.3 \pm 0.3$ meV, $\Gamma = 0.15 \pm 0.05$ meV, $J_2 = -0.19 \pm 0.15$ meV, and $J_3 = 1.35 \pm 0.15$ meV. The LL-simulated spectrum shows intensity at both the M and Γ points, although the intensity at Γ is lower than in the experiment. In addition, the simulation captures the curvature of the spin-wave dispersion along the $\Gamma \rightarrow M$ path as well as the feature at $\omega = 6$ meV. ED is subject to finite-size restrictions and low-momentum resolution, but captures the magnetic order and energy scale of the low-energy scattering ($\omega < 5$ meV).

How does our optimized solution compare to other proposed models for α-RuCl$_3$? Using the surrogates we can easily calculate $\hat{\chi}^2$ values for proposed models described by Eq. (1). By this metric our fit outperforms other models in the literature at describing the neutron data; see SM [21]. Our fit has a Kitaev interaction strength comparable with a previous INS fit [31] but lower Γ/K and higher J_3/K. However, the energy scale is generally smaller than for models predicted by band structure calculations and for models that seek to explain the experimental magnetic specific heat $C(T)$ [73]. Consequently, thermal pure quantum state [94,95] $C(T)$ results for the optimized solution fail to capture the experimentally observed high-temperature peak [21,49]. One of our identified near-optimized parameter sets performs better in this regard but worse at reproducing subtle spectral features [21]. This reinforces the point that Eq. (1) may miss some important term.

One limitation of our approach is the use of SCS. This was necessary to generate large amounts of training data and allowed us to generate phase diagrams. However, quantum effects can be significant close to phase boundaries, thus locally diminishing the reliability of our networks and requiring many-body verification. This is particularly important in α-RuCl$_3$, which is close to a phase transition under magnetic fields and where many Hamiltonian parameters matter.

Our optimized parameters are close to a transition between the Z.Z. and the Z.Z. (2D) orders, but using ED we fortunately find the SCS results are physical and correctly identify the ground state. In contrast, the recently proposed Hamiltonian of Ref. [70] is close to a transition between ferromagnetic (FM) and Z.Z. orders, and our SCS predicts FM, while ED finds Z.Z. This suggests it may be useful to retrain the networks using many-body simulations in regions close to phase boundaries to increase physical predictability.

Our analysis shows that subtle changes in parameters affect the spectra and ordering. This means that other Hamiltonian terms could also account for the results. This implies that zero-field neutron scattering is probably insufficient to constrain the model beyond the treatment here. For a more definitive understanding of α-RuCl$_3$, additional data are needed. Simulations of field dependence suggest that high-field spectroscopy measurements should be helpful here in disentangling the contributions of competing terms. Neutron scattering with its ability to capture wave vector and energy effects would be particularly valuable. Coanalysis of high-field data along with zero-field measurements used here, as well as other observable properties, can then be undertaken using the ML-based approach.

Conclusion. We have demonstrated that unsupervised ML-SCS methods can be used to solve the inverse scattering problem inherent to INS experiments, thereby extending previous methods to also account for dynamics. Our approach can be applied to a wide range of magnetic systems to obtain phase diagrams and fit the full 4D experimental scattering, as long as sufficient amounts of training data can be generated. For α-RuCl$_3$ we find a relatively flat fitness landscape, producing an uncertain fit. It does not fully explain the experimental scattering, likely due to interactions not considered here. Nevertheless, the optimal parameters reproduce many smaller scattering features, not captured by other proposed models. Improved algorithms are needed to extend the method further to even higher-dimensional parameter spaces and to fully constrain Hamiltonians. This can be done iteratively, building on previously simulated data. With future advances in computing power, we hope such methods may be used to rapidly and reliably identify the crucial physics of new materials.

[1] L. Balents, Spin liquids in frustrated magnets, Nature (London) **464**, 199 (2010).

[2] C. Lacroix, P. Mendels, and F. Mila, eds., *Introduction to Frustrated Magnetism: Materials, Experiments, Theory*, Springer Series in Solid-State Sciences (Springer-Verlag, Berlin, Heidelberg, 2011), Vol. 164.

[3] L. Savary and L. Balents, Quantum spin liquids: a review, Rep. Prog. Phys. **80**, 016502 (2017).

[4] K. W. Plumb, J. P. Clancy, L. J. Sandilands, V. V. Shankar, Y. F. Hu, K. S. Burch, H.-Y. Kee, and Y.-J. Kim, $\alpha - RuCl_3$: A spin-orbit assisted Mott insulator on a honeycomb lattice, Phys. Rev. B **90**, 041112(R) (2014).

[5] L. J. Sandilands, Y. Tian, K. W. Plumb, Y.-J. Kim, and K. S. Burch, Scattering Continuum and Possible Fractionalized Excitations in α–$RuCl_3$, Phys. Rev. Lett. **114**, 147201 (2015).

[6] A. Banerjee, C. A. Bridges, J.-Q. Yan, A. A. Aczel, L. Li, M. B. Stone, G. E. Granroth, M. D. Lumsden, Y. Yiu, J. Knolle, S. Bhattacharjee, D. L. Kovrizhin, R. Moessner, D. A. Tennant, D. G. Mandrus, and S. E. Nagler, Proximate Kitaev quantum spin liquid behaviour in a honeycomb magnet, Nat. Mater. **15**, 733 (2016).

[7] A. Banerjee, J. Yan, J. Knolle, C. A. Bridges, M. B. Stone, M. D. Lumsden, D. G. Mandrus, D. A. Tennant, R. Moessner, and S. E. Nagler, Neutron scattering in the proximate quantum spin liquid α-$RuCl_3$, Science **356**, 1055 (2017).

[8] S.-H. Do, S.-Y. Park, J. Yoshitake, J. Nasu, Y. Motome, Y. S. Kwon, D. T. Adroja, D. J. Voneshen, K. Kim, T.-H. Jang, J.-H. Park, K.-Y. Choi, and S. Ji, Majorana fermions in the Kitaev quantum spin system α-$RuCl_3$, Nat. Phys. **13**, 1079 (2017).

[9] K. Ran, J. Wang, W. Wang, Z.-Y. Dong, X. Ren, S. Bao, S. Li, Z. Ma, Y. Gan, Y. Zhang, J. T. Park, G. Deng, S. Danilkin, S.-L. Yu, J.-X. Li, and J. Wen, Spin-Wave Excitations Evidencing the Kitaev Interaction in Single Crystalline α–$RuCl_3$, Phys. Rev. Lett. **118**, 107203 (2017).

[10] A. Banerjee, P. Lampen-Kelley, J. Knolle, C. Balz, A. A. Aczel, B. Winn, Y. Liu, D. Pajerowski, J. Yang, C. A. Bridges, A. T. Savici, B. C. Chakoumakos, M. D. Lumsden, D. A. Tennant, R. Moessner, D. G. Mandrus, and S. E. Nagler, Excitations in the field-induced quantum spin liquid state of α-$RuCl_3$, npj Quantum Mater. **3**, 8 (2018).

[11] C. Balz, P. Lampen-Kelley, A. Banerjee, J. Yan, Z. Lu, X. Hu, S. M. Yadav, Y. Takano, Y. Liu, D. A. Tennant, M. D. Lumsden, D. Mandrus, and S. E. Nagler, Finite field regime for a quantum spin liquid in α–$RuCl_3$, Phys. Rev. B **100**, 060405(R) (2019).

[12] S. M. Winter, A. A. Tsirlin, M. Daghofer, J. van den Brink, Y. Singh, P. Gegenwart, and R. Valentí, Models and materials for generalized Kitaev magnetism, J. Phys.: Condens. Matter **29**, 493002 (2017).

[13] H. Takagi, T. Takayama, G. Jackeli, G. Khaliullin, and S. E. Nagler, Concept and realization of Kitaev quantum spin liquids, Nat. Rev. Phys. **1**, 264 (2019).

[14] Y. Motome and J. Nasu, Hunting Majorana fermions in Kitaev magnets, J. Phys. Soc. Jpn. **89**, 012002 (2020).

[15] A. Kitaev, Anyons in an exactly solved model and beyond, Ann. Phys. **321**, 2 (2006).

[16] M. Hermanns, I. Kimchi, and J. Knolle, Physics of the Kitaev model: Fractionalization, dynamic correlations, and material connections, Annu. Rev. Condens. Matter Phys. **9**, 17 (2018).

[17] C. Nayak, S. H. Simon, A. Stern, M. Freedman, and S. Das Sarma, Non-abelian anyons and topological quantum computation, Rev. Mod. Phys. **80**, 1083 (2008).

[18] D. Aasen, R. S. K. Mong, B. M. Hunt, D. Mandrus, and J. Alicea, Electrical Probes of the Non-Abelian Spin Liquid in Kitaev Materials, Phys. Rev. X **10**, 031014 (2020).

[19] K. Klocke, D. Aasen, R. S. K. Mong, E. A. Demler, and J. Alicea, Time-Domain Anyon Interferometry in Kitaev Honeycomb Spin Liquids and Beyond, Phys. Rev. Lett. **126**, 177204 (2021).

[20] J. G. Rau, E. K.-H. Lee, and H.-Y. Kee, Generic Spin Model for the Honeycomb Iridates beyond the Kitaev Limit, Phys. Rev. Lett. **112**, 077204 (2014).

[21] See Supplemental Material at http://link.aps.org/supplemental/10.1103/PhysRevResearch.4.L022061 for more details of the experiments and calculations.

[22] J. Chaloupka and G. Khaliullin, Magnetic anisotropy in the Kitaev model systems Na_2IrO_3 and $RuCl_3$, Phys. Rev. B **94**, 064435 (2016).

[23] C. Balz, L. Janssen, P. Lampen-Kelley, A. Banerjee, Y. H. Liu, J.-Q. Yan, D. G. Mandrus, M. Vojta, and S. E. Nagler, Field-induced intermediate ordered phase and anisotropic interlayer interactions in α–$RuCl_3$, Phys. Rev. B **103**, 174417 (2021).

[24] H. Suzuki, H. Liu, J. Bertinshaw, K. Ueda, H. Kim, S. Laha, D. Weber, Z. Yang, L. Wang, K. F. H. Takahash and, M. Minola, B. V. Lotsch, B. J. Kim, H. Yavaå, M. Daghofer, J. Chaloupka, G. Khaliullin, H. Gretarsson, and B. Keimer, Proximate ferromagnetic state in the Kitaev model material α-$RuCl_3$, Nat. Commun. **12**, 4512 (2021).

[25] J. A. Sears, M. Songvilay, K. W. Plumb, J. P. Clancy, Y. Qiu, Y. Zhao, D. Parshall, and Y.-J. Kim, Magnetic order in $\alpha - RuCl_3$: A honeycomb-lattice quantum magnet with strong spin-orbit coupling, Phys. Rev. B **91**, 144420 (2015).

[26] R. D. Johnson, S. C. Williams, A. A. Haghighirad, J. Singleton, V. Zapf, P. Manuel, I. I. Mazin, Y. Li, H. O. Jeschke, R. Valentí, and R. Coldea, Monoclinic crystal structure of $\alpha - RuCl_3$ and the zigzag antiferromagnetic ground state, Phys. Rev. B **92**, 235119 (2015).

[27] H. B. Cao, A. Banerjee, J.-Q. Yan, C. A. Bridges, M. D. Lumsden, D. G. Mandrus, D. A. Tennant, B. C. Chakoumakos, and S. E. Nagler, Low-temperature crystal and magnetic structure of $\alpha - RuCl_3$, Phys. Rev. B **93**, 134423 (2016).

[28] G. Jackeli and G. Khaliullin, Mott Insulators in the Strong Spin-Orbit Coupling Limit: From Heisenberg to a Quantum Compass and Kitaev Models, Phys. Rev. Lett. **102**, 017205 (2009).

[29] S. M. Winter, Y. Li, H. O. Jeschke, and R. Valentí, Challenges in design of Kitaev materials: Magnetic interactions from competing energy scales, Phys. Rev. B **93**, 214431 (2016).

[30] C. Eichstaedt, Y. Zhang, P. Laurell, S. Okamoto, A. G. Eguiluz, and T. Berlijn, Deriving models for the Kitaev spin-liquid candidate material α–RuCl$_3$ from first principles, Phys. Rev. B **100**, 075110 (2019).

[31] S. M. Winter, K. Riedl, P. A. Maksimov, A. L. Chernyshev, A. Honecker, and R. Valentí, Breakdown of magnons in a strongly spin-orbit coupled magnet, Nat. Commun. **8**, 1152 (2017).

[32] S. M. Winter, K. Riedl, D. Kaib, R. Coldea, and R. Valentí, Probing $\alpha - RuCl_3$ beyond Magnetic Order: Effects of Temperature and Magnetic Field, Phys. Rev. Lett. **120**, 077203 (2018).

[33] P. A. Maksimov and A. L. Chernyshev, Rethinking α–RuCl$_3$, Phys. Rev. Research **2**, 033011 (2020).

[34] J. Nasu, J. Knolle, D. L. Kovrizhin, Y. Motome, and R. Moessner, Fermionic response fram fractionalization in an insulating two-dimensional magnet, Nat. Phys. **12**, 912 (2016).

[35] L. Du, Y. Huang, Y. Wang, Q. Wang, R. Yang, J. Tang, M. Liao, D. Shi, Y. Shi, and X. Zhou, 2D proximate quantum spin liquid state in atomic-thin α-RuCl$_3$, 2D Mater. **6**, 015014 (2018).

[36] T. T. Mai, A. McCreary, P. Lampen-Kelley, N. Butch, J. R. Simpson, J.-Q. Yan, S. E. Nagler, D. Mandrus, A. R. H. Walker, and R. V. Aguilar, Polarization-resolved raman spectroscopy of α–RuCl$_3$ and evidence of room-temperature two-dimensional magnetic scattering, Phys. Rev. B **100**, 134419 (2019).

[37] Y. Wang, G. B. Osterhoudt, Y. Tian, P. Lampen-Kelley, A. Banerjee, T. Goldstein, J. Yan, J. Knolle, H. Ji, R. J. Cava, J. Nasu, Y. Motome, S. E. Nagler, D. Mandrus, and K. S. Burch, The range of non-Kitaev terms and fractional particles in α-RuCl$_3$, npj Quantum Mater. **5**, 14 (2020).

[38] J. Zheng, K. Ran, T. Li, J. Wang, P. Wang, B. Liu, Z.-X. Liu, B. Normand, J. Wen, and W. Yu, Gapless Spin Excitations in the Field-Induced Quantum Spin Liquid Phase of α–RuCl$_3$, Phys. Rev. Lett. **119**, 227208 (2017).

[39] S.-H. Baek, S.-H. Do, K.-Y. Choi, Y. S. Kwon, A. U. B. Wolter, S. Nishimoto, J. van den Brink, and B. Büchner, Evidence for a Field-Induced Quantum Spin Liquid in α-RuCl$_3$, Phys. Rev. Lett. **119**, 037201 (2017).

[40] J. A. Sears, Y. Zhao, Z. Xu, J. W. Lynn, and Y.-J. Kim, Phase diagram of $\alpha - RuCl_3$ in an in-plane magnetic field, Phys. Rev. B **95**, 180411(R) (2017).

[41] P. Czajka, T. Gao, M. Hirschberger, P. Lampen-Kelley, A. Banerjee, J. Yan, D. G. Mandrus, S. E. Nagler, and N. P. Ong, Oscillations of the thermal conductivity in the spin-liquid state of α-RuCl$_3$, Nat. Phys. **17**, 915 (2021).

[42] I. S. Villadiego, Pseudoscalar U(1) spin liquids in α–RuCl$_3$, Phys. Rev. B **104**, 195149 (2021).

[43] W. G. F. Krüger and L. Janssen, Nesting instability of gapless U(1) spin liquids with spinon Fermi pockets in two dimensions, Phys. Rev. B **104**, 165133 (2021).

[44] Y. Kasahara, T. Ohnishi, Y. Mizukami, O. Tanaka, S. Ma, K. Sugii, N. Kurita, H. Tanaka, J. Nasu, Y. Motome, T. Shibauchi, and Y. Matsuda, Majorana quantization and half-integer thermal quantum Hall effect in a Kitaev spin liquid, Nature (London) **559**, 227 (2018).

[45] M. Yamashita, J. Gouchi, Y. Uwatoko, N. Kurita, and H. Tanaka, Sample dependence of half-integer quantized thermal Hall effect in the Kitaev spin-liquid candidate α–RuCl$_3$, Phys. Rev. B **102**, 220404(R) (2020).

[46] T. Yokoi, S. Ma, Y. Kasahara, S. Kasahara, T. Shibauchi, N. Kurita, H. Tanaka, J. Nasu, Y. Motome, C. Hickey, S. Trebst, and Y. Matsuda, Half-integer quantized anomalous thermal Hall effect in the Kitaev material candidate α-RuCl$_3$, Science **373**, 568 (2021).

[47] H. Li, T. T. Zhang, A. Said, G. Fabbris, D. G. Mazzone, J. Q. Yan, D. Mandrus, G. B. Halász, S. Okamoto, S. Murakami, M. P. M. Dean, H. N. Lee, and H. Miao, Giant phonon anomalies in the proximate Kitaev quantum spin liquid α-RuCl$_3$, Nat. Commun. **12**, 3513 (2021).

[48] A. U. B. Wolter, L. T. Corredor, L. Janssen, K. Nenkov, S. Schönecker, S.-H. Do, K.-Y. Choi, R. Albrecht, J. Hunger, T. Doert, M. Vojta, and B. Büchner, Field-induced quantum criticality in the Kitaev system $\alpha - RuCl_3$, Phys. Rev. B **96**, 041405(R) (2017).

[49] S. Widmann, V. Tsurkan, D. A. Prishchenko, V. G. Mazurenko, A. A. Tsirlin, and A. Loidl, Thermodynamic evidence of fractionalized excitations in $\alpha - RuCl_3$, Phys. Rev. B **99**, 094415 (2019).

[50] S. Bachus, D. A. S. Kaib, Y. Tokiwa, A. Jesche, V. Tsurkan, A. Loidl, S. M. Winter, A. A. Tsirlin, R. Valentí, and P. Gegenwart, Thermodynamic Perspective on Field-Induced Behavior of α–RuCl$_3$, Phys. Rev. Lett. **125**, 097203 (2020).

[51] O. Tanaka, Y. Mizukami, R. Harasawa, K. Hashimoto, K. Hwang, N. Kurita, H. Tanaka, S. Fujimoto, Y. Matsuda, E.-G. Moon, and T. Shibauchi, Thermodynamic evidence for a field-angle-dependent Majorana gap in a Kitaev spin liquid, Nat. Phys. **18**, 429 (2022).

[52] N. Janša, A. Zorko, M. Gomilšek, M. Pregelj, K. W. Krämer, D. Biner, A. Biffin, C. Rüegg, and M. Klanjšek, Observation of two types of fractional excitation in the Kitaev honeycomb magnet, Nat. Phys. **14**, 786 (2018).

[53] A. N. Ponomaryov, L. Zviagina, J. Wosnitza, P. Lampen-Kelley, A. Banerjee, J.-Q. Yan, C. A. Bridges, D. G. Mandrus, S. E. Nagler, and S. A. Zvyagin, Nature of Magnetic Excitations in the High-Field Phase of α–RuCl$_3$, Phys. Rev. Lett. **125**, 037202 (2020).

[54] C. Wellm, J. Zeisner, A. Alfonsov, A. U. B. Wolter, M. Roslova, A. Isaeva, T. Doert, M. Vojta, B. Büchner, and V. Kataev, Signatures of low-energy fractionalized excitations in α–RuCl$_3$ from field-dependent microwave absorption, Phys. Rev. B **98**, 184408 (2018).

[55] D. Hirobe, M. Sato, Y. Shiomi, H. Tanaka, and E. Saitoh, Magnetic thermal conductivity far above the Néel temperature in the Kitaev-magnet candidate α–RuCl$_3$, Phys. Rev. B **95**, 241112(R) (2017).

[56] Y. Kasahara, K. Sugii, T. Ohnishi, M. Shimozawa, M. Yamashita, N. Kurita, H. Tanaka, J. Nasu, Y. Motome, T. Shibauchi, and Y. Matsuda, Unusual Thermal Hall Effect in a Kitaev Spin Liquid Candidate α–RuCl$_3$, Phys. Rev. Lett. **120**, 217205 (2018).

[57] A. Little, L. Wu, P. Lampen-Kelley, A. Banerjee, S. Patankar, D. Rees, C. A. Bridges, J.-Q. Yan, D. Mandrus, S. E. Nagler, and J. Orenstein, Antiferromagnetic Resonance and Terahertz Continuum in α–RuCl$_3$, Phys. Rev. Lett. **119**, 227201 (2017).

[58] Z. Wang, S. Reschke, D. Hüvonen, S.-H. Do, K.-Y. Choi, M. Gensch, U. Nagel, T. Rõõm, and A. Loidl, Magnetic Excitations

and Continuum of a Possibly Field-Induced Quantum Spin Liquid in α–RuCl$_3$, Phys. Rev. Lett. **119**, 227202 (2017).

[59] L. Wu, A. Little, E. E. Aldape, D. Rees, E. Thewalt, P. Lampen-Kelley, A. Banerjee, C. A. Bridges, J.-Q. Yan, D. Boone, S. Patankar, D. Goldhaber-Gordon, D. Mandrus, S. E. Nagler, E. Altman, and J. Orenstein, Field evolution of magnons in α–RuCl$_3$ by high-resolution polarized terahertz spectroscopy, Phys. Rev. B **98**, 094425 (2018).

[60] I. O. Ozel, C. A. Belvin, E. Baldini, I. Kimchi, S. Do, K.-Y. Choi, and N. Gedik, Magnetic field-dependent low-energy magnon dynamics in $\alpha - $RuCl$_3$, Phys. Rev. B **100**, 085108 (2019).

[61] S. Reschke, V. Tsurkan, S.-H. Do, K.-Y. Choi, P. Lunkenheimer, Z. Wang, and A. Loidl, Terahertz excitations in α–RuCl$_3$: Majorana fermions and rigid-plane shear and compression modes, Phys. Rev. B **100**, 100403(R) (2019).

[62] J. Cookmeyer and J. E. Moore, Spin-wave analysis of the low-temperature thermal Hall effect in the candidate Kitaev spin liquid $\alpha - $RuCl$_3$, Phys. Rev. B **98**, 060412(R) (2018).

[63] H.-S. Kim, V. S. V., A. Catuneanu, and H.-Y. Kee, Kitaev magnetism in honeycomb RuCl$_3$ with intermediate spin-orbit coupling, Phys. Rev. B **91**, 241110(R) (2015).

[64] H.-S. Kim and H.-Y. Kee, Crystal structure and magnetism in $\alpha - $RuCl$_3$: An ab initio study, Phys. Rev. B **93**, 155143 (2016).

[65] R. Yadav, N. A. Bogdanov, V. M. Katukuri, S. Nishimoto, J. van den Brink, and L. Hozoi, Kitaev exchange and field-induced quantum spin-liquid states in honeycomb α-RuCl$_3$, Sci. Rep. **6**, 37925 (2016).

[66] T. Suzuki and S.-i. Suga, Effective model with strong Kitaev interactions for α–RuCl$_3$, Phys. Rev. B **97**, 134424 (2018).

[67] T. Suzuki and S.-i. Suga, Erratum: Effective model with strong Kitaev interactions for α–RuCl$_3$ [Phys. Rev. B 97, 134424 (2018)], Phys. Rev. B **99**, 249902(E) (2019).

[68] Y. S. Hou, H. J. Xiang, and X. G. Gong, Unveiling magnetic interactions of ruthenium trichloride via constraining direction of orbital moments: Potential routes to realize a quantum spin liquid, Phys. Rev. B **96**, 054410 (2017).

[69] W. Wang, Z.-Y. Dong, S.-L. Yu, and J.-X. Li, Theoretical investigation of magnetic dynamics in $\alpha - $RuCl$_3$, Phys. Rev. B **96**, 115103 (2017).

[70] H. Li, H.-K. Zhang, J. Wang, H.-Q. Wu, Y. Gao, D.-W. Qu, Z.-X. Liu, S.-S. Gong, and W. Li, Identification of magnetic interactions and high-field quantum spin liquid in α-RuCl$_3$, Nat. Commun. **12**, 4007 (2021).

[71] K. Ran, J. Wang, S. Bao, Z. Cai, Y. Shangguan, Z. Ma, W. Wang, Z.-Y. Dong, P. ermk, A. Schneidewind, S. Meng, Z. Lu, S.-L. Yu, J.-X. Li, and J. Wen, Evidence for magnetic fractional excitations in a Kitaev quantum-spin-liquid candidate α-RuCl$_3$, Chin. Phys. Lett. **39**, 027501 (2022).

[72] L. Janssen, E. C. Andrade, and M. Vojta, Magnetization processes of zigzag states on the honeycomb lattice: Identifying spin models for α–RuCl$_3$ and Na$_2$IrO$_3$, Phys. Rev. B **96**, 064430 (2017).

[73] P. Laurell and S. Okamoto, Dynamical and thermal magnetic properties of the Kitaev spin liquid candidate α-RuCl$_3$, npj Quantum Mater. **5**, 2 (2020).

[74] P. Mehta, M. Bukov, C.-H. Wang, A. G. Day, C. Richardson, C. K. Fisher, and D. J. Schwab, A high-bias, low-variance introduction to machine learning for physicists, Phys. Rep. **810**, 1 (2019).

[75] J. Carrasquilla, Machine learning for quantum matter, Adv. Phys. X **5**, 1797528 (2020).

[76] M. Doucet, A. M. Samarakoon, C. Do, W. T. Heller, R. Archibald, D. A. Tennant, T. Proffen, and G. E. Granroth, Machine learning for neutron scattering at ORNL, Mach. Learn.: Sci. Technol. **2**, 023001 (2021).

[77] K. T. Butler, M. D. Le, J. Thiyagalingam, and T. G. Perring, Interpretable, calibrated neural networks for analysis and understanding of inelastic neutron scattering data, J. Phys.: Condens. Matter **33**, 194006 (2021).

[78] Z. Chen, N. Andrejevic, N. C. Drucker, T. Nguyen, R. P. Xian, T. Smidt, Y. Wang, R. Ernstorfer, D. A. Tennant, M. Chan, and M. Li, Machine learning on neutron and x-ray scattering and spectroscopies, Chem. Phys. Rev. **2**, 031301 (2021).

[79] S. Yu, Y. Gao, B.-B. Chen, and W. Li, Learning the effective spin Hamiltonian of a quantum magnet, Chin. Phys. Lett. **38**, 097502 (2021).

[80] A. Tennant and A. Samarakoon, Machine learning for magnetic phase diagrams and inverse scattering problems, J. Phys.: Condens. Matter **34**, 044002 (2021).

[81] A. M. Samarakoon, K. Barros, Y. W. Li, M. Eisenbach, Q. Zhang, F. Ye, V. Sharma, Z. L. Dun, H. Zhou, S. A. Grigera, C. D. Batista, and D. A. Tennant, Machine learning assisted insight to spin ice Dy$_2$ Ti$_2$ O$_7$, Nat. Commun. **11**, 892 (2020).

[82] T. E. Mason, D. Abernathy, I. Anderson, J. Ankner, T. Egami, G. Ehlers, A. Ekkebus, G. Granroth, M. Hagen, K. Herwig, J. Hodges, C. Hoffmann, C. Horak, L. Horton, F. Klose, J. Larese, A. Mesecar, D. Myles, J. Neuefeind, M. Ohl *et al.*, The Spallation Neutron Source in Oak Ridge: A powerful tool for materials research, Phys. B: Condens. Matter **385-386**, 955 (2006).

[83] S. Rosenkranz and R. Osborn, Corelli: Efficient single crystal diffraction with elastic discrimination, Pramana - J. Phys. **71**, 705 (2008).

[84] G. E. Granroth, D. H. Vandergriff, and S. E. Nagler, SEQUOIA: A fine resolution chopper spectrometer at the SNS, Phys. B: Condens. Matter **385-386**, 1104 (2006).

[85] G. E. Granroth, A. I. Kolesnikov, T. E. Sherline, J. P. Clancy, K. A. Ross, J. P. C. Ruff, B. D. Gaulin, and S. E. Nagler, SEQUOIA: A newly operating chopper spectrometer at the SNS, J. Phys.: Conf. Ser. **251**, 012058 (2010).

[86] L. Janssen, S. Koch, and M. Vojta, Magnon dispersion and dynamic spin response in three-dimensional spin models for α–RuCl$_3$, Phys. Rev. B **101**, 174444 (2020).

[87] K. Liu, N. Sadoune, N. Rao, J. Greitemann, and L. Pollet, Revealing the phase diagram of Kitaev materials by machine learning: Cooperation and competition between spin liquids, Phys. Rev. Research **3**, 023016 (2021).

[88] N. Rao, K. Liu, M. Machaczek, and L. Pollet, Machine-learned phase diagrams of generalized Kitaev honeycomb magnets, Phys. Rev. Research **3**, 033223 (2021).

[89] N. Metropolis, A. W. Rosenbluth, M. N. Rosenbluth, A. H. Teller, and E. Teller, Equation of state calculations by fast computing machines, J. Chem. Phys. **21**, 1087 (1953).

[90] T. Huberman, D. A. Tennant, R. A. Cowley, R. Coldea, and C. D. Frost, A study of the quantum classical crossover in the spin dynamics of the 2D $S = 5/2$ antiferromagnet Rb$_2$ MnF$_4$:

neutron scattering, computer simulations and analytic theories, J. Stat. Mech.: Theory Exp. (2008) P05017.

[91] D. R. Jones, M. Schonlau, and W. J. Welch, Efficient global optimization of expensive black-box functions, J. Glob. Optim. **13**, 455 (1998).

[92] D. S. Broomhead and D. Lowe, Radial basis functions, multi-variable functional interpolation and adaptive networks, Memorandum Rep. No. 4148 (Royal Signals and Radar Establishment Malvern, United Kingdom, 1988).

[93] A. M. Samarakoon, D. A. Tennant, F. Ye, Q. Zhang, and S. A. Grigera, Integration of machine learning with neutron scattering: Hamiltonian tuning in spin ice with pressure, (2021), arXiv:2110.15817.

[94] S. Sugiura and A. Shimizu, Thermal Pure Quantum States at Finite Temperature, Phys. Rev. Lett. **108**, 240401 (2012).

[95] M. Kawamura, K. Yoshimi, T. Misawa, Y. Yamaji, S. Todo, and N. Kawashima, Quantum lattice model solver $\mathcal{H}\phi$, Comput. Phys. Commun. **217**, 180 (2017).